Turbidite deposition and diagenesis in the southwestern Black Sea: Implications for biogeochemical cycling in an anoxic basin

Peter Kraal[a,*,1], Mustafa Yücel[b], Caroline P. Slomp[a]

[a] Department of Earth Sciences – Geochemistry, Faculty of Geosciences, Utrecht University, PO Box 80021, Utrecht, TA 3508, the Netherlands
[b] Institute of Marine Sciences, Middle East Technical University, Erdemli, Mersin 33731, Turkey

ABSTRACT

The biogeochemical cycles of iron, phosphorus and sulfur are intimately linked and the fate of these elements is highly redox-dependent. Under anoxic conditions, iron is reduced to Fe(II), for an important part driven by reaction with sulfide. Reduction and sulfidation diminish the affinity of iron for phosphorus, thereby affecting sedimentary phosphorus retention. The coupled cycling of iron-phosphorus-sulfur as a function of redox conditions thereby helps control nutrient availability and primary productivity in marine systems. The Black Sea is the world's largest permanently stratified basin with a strong gradient from oxic surface waters to anoxic and strongly sulfidic deep waters, and is therefore well-suited to investigate redox-dependent changes in coupled iron-phosphorus-sulfur cycling. The presence of sulfide in the deep Black Sea alters the chemical speciation of iron (Fe) and phosphorus (P) in particulate matter in the water column and sediment. These alterations and their impact are poorly constrained for turbidites, which are deposits formed by mass transport from the continental slope into the deep basin of the Black Sea through turbidity currents. Here, we compare the geochemistry of sediments on the southwestern (SW) Black Sea slope overlain by oxygenated waters (234 m below sea surface, mbss) with that of a sediment record with turbidite intervals from the sulfidic SW deep basin (2169 mbss). The aims were to investigate the potential of SW slope sediment as source material for turbidites, and to assess the geochemical impact of reaction with sulfide. The bulk chemistry (Al, CaCO$_3$, Fe) of the SW deep Black Sea turbidite intervals was similar to that of SW Black Sea slope sediments (234 m water depth), suggesting that the latter are source material for deep SW Black Sea turbidites. The source sediment is characterized by strong enrichments in highly reactive Fe(III) and Mn phases, high rates of sulfate reduction and the presence of methane. Similar total Fe contents in the slope and deep turbidite sediments suggest that Fe is efficiently retained in the sediment. In contrast, Mn is depleted during down-slope transport and P contents in the turbidite intervals are about 50% lower than in the slope sediment, indicating significant P release during and after turbidite deposition. Calculations using the obtained data and conservative estimates of the areal extent of turbidite deposition in the SW Black Sea indicate that turbidity currents have the potential to impact coupled Fe-P-S biogeochemical cycling by boosting Fe input, dissolved P accumulation, sulfide oxidation and FeS$_2$ burial in the deep Black Sea.

1. Introduction

The Black Sea is the world's largest marine basin with permanently anoxic deep waters. A stable density stratification inhibits mixing between the relatively fresh, well-mixed surface waters and the more saline deep waters. This stratification results in the loss of dissolved O$_2$ below 70–100 m water depth (mbss) and the accumulation of dissolved sulfide (HS$^-$) up to concentrations of $\sim 400\,\mu\mathrm{mol}\,L^{-1}$ in the deepest waters (> 2000 mbss) (Sorokin 1983; Codispoti et al. 1991). The stratified water column was formed during Late Glacial warming, when sea level rose and relatively dense, saline Mediterranean waters entered the Black Sea basin (Degens and Ross 1974). Deep Black Sea bottom waters have been anoxic and sulfidic for thousands of years (Wilkin et al. 1997). Because of this characteristic, the Black Sea is widely used as a model anoxic basin to study biogeochemical cycling under long-term oxygen depletion.

The cycling and fate of iron (Fe) in the Black Sea has received extensive attention. Iron is an essential trace element that limits productivity in large areas of Earth's marine realm, and also impacts the biogeochemical cycling of other essential elements through sorption and coprecipitation processes (Boyd and Ellwood 2010; Boyd et al. 2017; Tagliabue et al. 2017). In the Black Sea, redox conditions in the water column control sedimentary Fe speciation and retention; under oxic conditions Fe is efficiently sequestered in Fe(III) (oxyhydr)oxides while sulfidic conditions lead to sequestration as Fe(II) sulfides (FeS$_x$). Intermediate, anoxic but non-sulfidic conditions can promote Fe^{2+} mobilization by reductive dissolution of Fe(III), thus lowering the sedimentary retention capacity for Fe (Scholz et al. 2014a). Because of the strong coupling between sediment Fe chemistry and bottom water redox conditions, sedimentary Fe records are often used to reconstruct paleo-depositional redox conditions (Raiswell and Berner 1985; Raiswell and Canfield 1998; Poulton and Canfield 2011; Hardisty et al.

2018; Scholz 2018). In the Black Sea, the shelf supplies reactive Fe through lateral transport of particulate Fe (clay-associated Fe and/or Fe(III) precipitates formed by oxidation of the sedimentary dissolved Fe^{2+} efflux in shelf bottom waters) to the deep basin, where it undergoes sulfidation and is permanently buried as FeS_2 (Canfield et al. 1996; Lyons 1997; Dijkstra et al. 2018b; Lenstra et al. 2018). This process enriches deep basin sediments with shelf-derived Fe (Wijsman et al. 2001; Lyons and Severmann 2006; Severmann et al. 2008). Such Fe enrichments have been used as a tool to determine paleo-environmental conditions in the Black Sea and the associated strength of the Fe shuttle (Eckert et al. 2013). A similar shuttling mechanism has been observed in other basins with sulfidic deep waters (Jilbert and Slomp 2013; Scholz et al. 2014b; Lenz et al. 2015).

A second mode of Fe transport from the shelf and slope into the deep basin, one that is only poorly understood, is by turbidity currents, downslope flows of sediment suspensions that form turbidites upon deposition. In the northwest (NW) Black Sea, turbidites are the result of slope instability in the fan complexes of the major rivers (Danube, Dniepr/Dniestr) (Lericolais et al. 2013). In the southwest (SW) Black Sea, seismic activity along the southern Black Sea margin associated with regional fracture zones (most notably the North Anatolian Fault) leads to earthquake-induced mass movements and turbidites (Konuk et al. 1991; Konovalov et al. 2007; Yücel et al. 2010b). Turbidite-associated Fe transport and deposition differs fundamentally from the shelf-to-basin Fe shuttle. The latter represents a supply of shelf-derived, reactive particulate Fe(III) that is sulfidized before reaching the sediment surface (Lyons 1997; Kraal et al. 2017; Dijkstra et al. 2018b). By contrast, turbidity currents have the potential to rapidly transport shelf sediments enriched in highly reactive particulate Fe(III) to the deep sea floor, where diagenesis under sulfidic conditions ensues (Lyons and Berner 1992; Yücel et al. 2010b; Dijkstra et al. 2014). The input of Fe(III) into sulfidic deep waters by turbidity currents boosts HS^- oxidation and FeS_2 formation, to an extent that it can significantly affect the deep Black Sea S cycle (Yücel et al. 2010b).

However, the geochemistry of potential turbidite source sediments is largely unknown. Lyons and Berner (1992) suggested anoxic/sulfidic black muds as a source of turbidite layers in the anoxic deep basin of the Black Sea with little change in the degree of sulfidation of the source material during transport and deposition. Overall, little is known about the initial abundance and reactivity of sedimentary Fe(III) phases entrained in turbidity currents, as well as the fate of other elements such as manganese (Mn) and phosphorus (P) during and after transport. Here, we report on SW Black Sea slope sediments that may serve as source material for turbidites and compare the geochemical characteristics – bulk chemistry, pore-water composition, chemical Fe and P speciation – to those of a deep SW Black Sea sediment record containing multiple turbidite intervals. We provide the first detailed solid-phase characterization of SW slope sediments and explore the impact of mass movement of such sediment on the geochemical cycling of Fe, Mn, P and S relative to the other depositional fluxes of these elements in the Black Sea.

2. Materials and methods

2.1. Water column and sediment sampling

The water column and surface sediment at shelf, slope and deep stations in the western Black Sea were sampled in June 2013 on a research cruise with R/V Pelagia. Here, we focus on two stations, one from the SW slope and one from the SW deep basin (Fig. 1, Table 1). Physical properties of the water column were measured with a temperature-conductivity-density (CTD) profiler, to which a Seabird SBE43 oxygen sensor was attached for dissolved O_2 measurements. Water column samples were taken at each station at selected depths using a sampling rosette equipped with 24 Niskin bottles. After retrieval, the water in the CTD rosette bottles was immediately sampled.

Multicores at the stations were collected using polycarbonate tubes of 60 cm length with an inner diameter of 10 cm. Approximately 50 cm of sediment was recovered with overlying water. General sediment properties and a generalized core description based on visual inspection are presented in Table 1. After ensuring that the sediment surface was undisturbed, a 20 mL sample of the overlying water was taken (for treatment and analyses as for pore-water samples, described below) and the cores were subsequently capped with rubber stoppers. At station 1, one core was then vertically transferred into a N_2-purged anaerobic chamber. The remaining overlying water was siphoned off, and the sediment core was sectioned into intervals between 0.5 and 4 cm thickness, with the resolution decreasing with sediment depth. About 15 mL of wet sediment from each interval was transferred into a pre-weighed glass vial that was stored in an anoxic jar at -20 °C prior to the on-shore water content determination and solid-phase analyses. The remaining material was transferred into 50 mL polypropylene centrifuge tubes for pore-water extraction. The closed centrifuge tubes were centrifuged at 4500 rpm for 20 min, and immediately transferred back into the anoxic glovebox where the supernatant was filtered through a 0.45 μm Teflon filter. At Station 13, the capped core was sampled with 20 mL syringes at 4 cm resolution through pre-drilled holes in the core tube. The syringes were immediately sealed with Parafilm M and transferred into the glovebox. Here, the syringes were extruded into 50 mL polypropylene centrifuge tubes. Pore-water was obtained using the abovementioned procedure, and the sediment residue was stored at -20 °C prior to solid-phase analyses.

A separate core for each station was used for methane (CH_4) analysis. Methane samples were taken from a predrilled core directly upon core retrieval. Precisely 10 mL of wet sediment was extracted from each hole with a plastic syringe and immediately transferred into a 65-mL glass bottle filled with saturated NaCl solution, sealed with a rubber stopper and a screw cap, and subsequently stored upside-down.

2.2. Voltammetric porewater micro-profiling

One additional core from each station was analyzed using a three-electrode voltammetric sensor with a gold amalgam (Au/Hg) voltammetric glass microelectrode as working electrode (Luther et al., 1998). This approach allows simultaneous determination of dissolved pore-water redox species such as O_2, HS^-/H_2S, thiosulfate ($S_2O_3^{2-}$), polysulfide (S_x^{2-}), elemental sulfur (S^0), manganese (Mn^{2+}), ferrous Fe^{2+} and qualitative detection of soluble iron monosulfide ($FeS_{(aq)}$) and ferric Fe^{3+} (Brendel and Luther, 1995; Luther et al., 2008; Taillefert et al., 2007). The three-electrode cell was calibrated separately for O_2, Mn^{2+}, Fe^{2+} and H_2S before the first application, using standard additions and Mn(II) was used as a pilot ion for subsequent calibrations (Konovalov et al., 2007; Yücel, 2013).

The sediment cores were profiled on board within 1 h after multicores were on deck. The Au/Hg glass working electrode was attached to a micromanipulator with counter and reference electrodes placed in the overlying water of the core. Then, the working electrode was vertically lowered vertically with at a depth resolution of at least 0.25 mm. Following the depth manipulation, four voltammetric scans were taken. The electrodes were connected to a benchtop potentiostat (DLK-60, AIS, Inc.) for data acquisition. The scans were taken in cyclic voltammetry mode from -0.1 V to -1.8 V and back at a rate of $1000\,mV\,sec^{-1}$. Before each scan, the electrode was conditioned at -0.9 V for 10 s to remove any adsorbed species. The concentrations were calculated using triplicate measurements after discarding the first scan, standard deviations were < 5%. Detection limits (DL) were $20\,\mu mol\,L^{-1}$ for O_2, $10\,\mu mol\,L^{-1}$ for Mn^{2+} and Fe^{2+} and $0.2\,\mu mol\,L^{-1}$ for ΣH_2S ($H_2S + HS^- + FeS_{(aq)}$). Sulfide as reported for the voltammetric analyses thus includes $FeS_{(aq)}$.
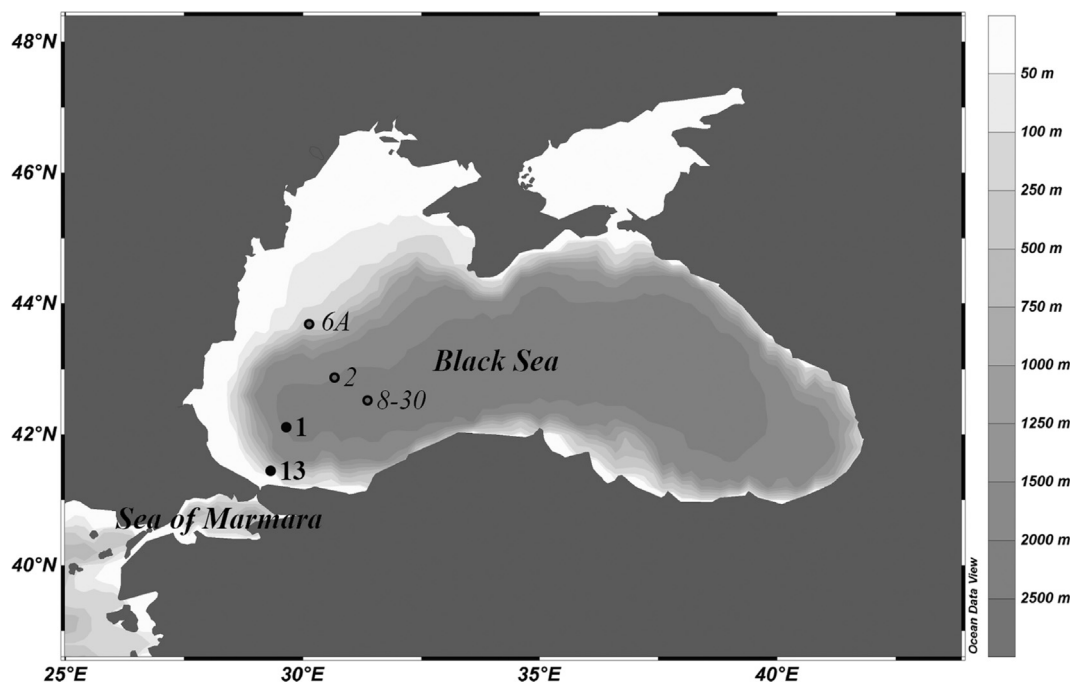
Fig. 1. Bathymetric map of the Black Sea with station locations. Black dots mark station 13 (234 mbss) and 1 (2169 mbss) in the southwest Black Sea that are the subject of the current study. Black-grey dots mark stations 6A (120 mbss) and 2 (2107 mbss) in the northwest Black Sea, discussed in detail in Kraal et al. (2017) and used here for comparing transport and transformation processes in different areas of the western Black Sea. Additionally, the location of station 8–30 with turbidite from Yücel et al. (2010b) is indicated.

2.3. Chemical analysis of water column and sediment samples

Samples from the CTD/rosette were filtered (0.45 μm Nylon filter membrane) and analyzed on-board for dissolved phosphate (PO_4^{3-}), sulfide ($HS^- + H_2S$, denoted here as HS^-), ammonium (NH_4^+), nitrate (NO_3^-) and nitrite (NO_2^-) with QuAAtro gas-segmented continuous flow analyzers (Seal Analytical) (Murphy and Riley 1962; Helder and De Vries 1979; Grashoff et al. 1983).

Various aliquots of pore-water were taken (in the anoxic glovebox) from the bulk pore-water sample for analyses (Table 2). Dissolved PO_4^{3-}, NH_4^+, NO_2^-, NO_3^-, HS^- and inorganic carbon (DIC) were quantified on-board within 16 h of sampling with a QuAAtro auto-analyzer (Seal Analytical). The aliquot for sulfide analysis was transferred into 8 mmol L^{-1} NaOH immediately after filtration to minimize loss of H_2S. Dissolved sulfate (SO_4^{2-}) concentrations were measured by ion chromatography (Dionex ICS-3000) on-shore at Utrecht University. Saturation indices for pertinent mineral phases were calculated using Visual MINTEQ 3.1.

On shore, a headspace of 10 mL of nitrogen was injected into the

Table 2
Pore-water sample treatment and analysis.

Analyte (sample volume)	Pre-treatment	Storage	Measurement
HPO_4^{2-}	Acidified to pH ~1 with 5 M suprapur HCl	4 °C	Autoanalyzer (on-board)
NH_4^+, NO_2^-, NO_3^-	None	4 °C	Autoanalyzer (on-board)
HS^-	Diluted 4 × in degassed 8 mmol L^{-1} NaOH	4 °C	Autoanalyzer (on-board)
DIC	Diluted 10 × in degassed 25 g L^{-1} NaCl	4 °C	Autoanalyzer (on-board)
SO_4^{2-}	Diluted 10 × in ultrapure water	4 °C	Ion chromatography (Utrecht Univ.)

CH_4 samples and CH_4 concentrations in the headspace were determined by injection of a subsample into a Thermo Finnigan Trace GC gas chromatograph equipped with a flame ionization detector (FID). The column operated at 50 °C, with 3 mL min^{-1} He flow as carrier gas. The

Table 1
General properties of coring locations and retrieved cores (BW = bottom water), listed by increasing water depth. The original station numbers were kept for easy comparison with studies from the same research expedition. Temperature from CTD profiler, oxygen and sulfide from the deepest Niskin bottle of CTD/Rosette sampler (depth between parentheses). Stations 6A and 2 from Kraal et al. (2017) are included for comparison, see Section 4.1.

Station	Coordinates (lat., long.)	Depth (mbss)	BW T (°C)	BW O$_2$ (μmol kg^{-1})	BW HS$^-$ (μmol L^{-1})	Core length (cm)	Sediment description
13 (SW slope)	41°27.8′ N 29°16.7′ E	234	8.8	7.1 (218 mbss)	0	47	Grey to dark-grey, fine-grained sediment (mud/silt based on visual observation)
1 (SW deep)	42°4.8′ N 29°40.7′ E	2169	9.1	b.d.[a] (2000 mbss)	396	54	Alternation of normal laminated marine mud with fine-grained homogeneous turbidite intervals
6A (NW slope)	43°44.10 N 30°04.40 E	120	8.5	10.7 (125 mbss [b])	0	26	Grey clay with shell banks, brown surface layer
2 (NW deep)	42°4.80 N 29°40.70 E	2107	9.1	b.d.[b] (2000 mbss)	418	36	Laminated mud with fluffy top layer

[a] Below the detection limit of O$_2$ sensor of ~ 0.5 ± 5 μmol kg^{-1}.
[b] CTD depth deeper than station depth; coring location was shifted slightly after CTD.

FID operated at 250 °C using a 1:10 H_2/air mixture. For sample analysis, 100 μL of sample in a Hamilton syringe with a stainless steel needle was introduced into the injector through a butyl rubber septum. The CH_4 concentration in the sample was calculated from the CH_4 peak area measured by FID, using a calibration line obtained by measuring peak areas for known amounts of CH_4 using analytical-grade CH_4 standards supplied by Westfalen AG.

Also on-shore, the frozen wet sediment samples in the glass vials (Station 1) or polypropylene tubes (Station 13) were freeze-dried and weighed to determine the water content from the mass loss during freeze-drying. Initial water content could not be determined for Station 13 samples, as these were centrifuge residues with unknown amounts of remaining pore-water. All freeze-dried sediment samples were manually ground in an N_2-filled glovebox with an agate mortar and pestle. A 0.3 g subsample of the ground sediment was decalcified by two washes with 1 M HCl (4 h and 12 h) followed by two rinses with ultrapure water. The sediment residue was freeze-dried and organic carbon (C_{org}) content was quantified with a CNS analyzer (Fisons Instruments NA 1500). A second subsample of 0.125 g was used for acid digestion. The subsample was digested in 5 mL of a mixture of concentrated HNO_3, $HClO_4$ and HF at 90 °C. After evaporation of these acids at 160 °C, the residue was dissolved overnight at 90 °C in 1 M HNO_3, and Al, Ca, Fe, Mn, P and S were determined by ICP-OES (Perkin Elmer Optima 3000). Calcium carbonate was calculated on a weight basis from total Ca contents after correction for clay-associated Al: $CaCO_3 = 2.5 \times (Ca - 0.345 \times Al)$ (Turekian and Wedepohl 1961; Reichart et al. 1997).

2.4. Resin embedding of station 1 sediment

A separate multicore from station 1 (2169 mbss) was stored upright at 4 °C until return to shore and used for resin embedding under anoxic conditions following the method of Jilbert and Slomp (2013): the uppermost, unconsolidated sediment (0–7 cm) was sampled in a 1-cm-diameter polypropylene tube from an upright core in a N_2-filled glovebag. Subsequently, the core was taken out of the glovebag and placed horizontally, cut in half length-wise and the sediment was sampled using aluminum (Al) trays (dimensions 20 × 2 × 1 cm) with 2.5 cm vertical overlap. The core-top samples and the sediments in the Al trays were embedded in epoxy-resin in an anoxic glovebox. The core-top samples were kept upright throughout the embedding procedure. The resin-embedded sediment blocks were polished with 0.3 μm aluminum oxide powder (as a fluid suspension between the blocks and a rotating stage). The resin blocks were cut in 5-cm blocks (at 30° angle) and scanned using a Canon CanoScan LiDE 210 color scanner.

2.5. Sequential chemical iron, phosphorus and sulfur extractions

Two separate subsamples of the ground sediment of 50 and 100 mg were used for sequential Fe and P extraction, respectively. The extraction steps and target Fe and P phases are detailed in Tables 3 and 4. The Fe and P extractions were performed under anoxic conditions to prevent artifacts due to sample oxidation (Kraal et al. 2009; Kraal and Slomp 2014).

The P concentrations in all extracts except the buffered citrate-dithionite extracts were measured with the molybdenum blue colorimetric method (Murphy and Riley 1962). The citrate-dithionite extracts were analyzed for Ca, Fe, Mn and P by ICP-OES. Reactive P was calculated by subtraction of detrital P (i.e. terrigenous unreactive P phases) from the total P pool.

After Fe extraction, the total Fe concentration in all extracts was determined with the colorimetric phenanthroline method (APHA 2005). In the HCl extracts from step 1 of the Fe extraction procedure, Fe^{2+} and total Fe were determined by measuring absorbance before and after adding the hydroxylamine-hydrochloride reducing agent that converts any dissolved Fe^{3+} to Fe^{2+}. The Fe^{3+} concentration was then calculated by difference.

The sum of the extracted Fe phases listed in Table 4 is termed highly reactive Fe (Fe_{HR}): iron that may interact with pore-water reductants (most importantly, HS^-) on geologically short timescales of years to millennia (Canfield et al. 1992; Raiswell and Canfield 1998; Poulton and Canfield 2005). Dissolution of magnetite in the HCl and CDB solutions (step 1 and 2 of sequential Fe extraction) is poorly constrained, therefore CDB-Fe and oxalate-Fe are collectively referred to as crystalline Fe(III) (oxyhydr)oxides (ox-Fe). The difference between total Fe as measured by acid digestion and the sum of the extracted Fe phases represents poorly reactive and unreactive Fe. The degree of pyritization (DOP) was calculated as the fraction of highly reactive Fe that was present as pyrite-Fe: $DOP = pyrite\text{-}Fe/Fe_{HR}$, a slight alteration of the original formulation of $DOP = pyrite\text{-}Fe/(pyrite\text{-}Fe + acid\text{-}soluble\ Fe)$ (Berner 1970; Raiswell et al. 1988).

A small subset of samples from station 1 was subjected to sequential extraction of acid-volatile sulfide, elemental sulfur (S^0) and pyrite-S as detailed in Kraal et al. (2013).

3. Results

3.1. Sediment type and composition

Visual observation of the resin-embedded sediment from SW deep station 1 (2169 mbss) showed a predominantly homogeneous, dark grey matrix with intercalated thin intervals of laminated (dark/light) sediment. This alternation, an example of which is shown in Fig. 2, reflects deposition of regular laminated sediment (i.e. from vertical settling fluxes) alternating with homogeneous sediment deposited by turbidity currents. In the upper ∼ 20 cm of the sediment record from station 1 – the section of the core that was sampled at relatively high resolution for chemical analysis, these alternations were also reflected in compositional changes: turbidite intervals were relatively rich in Al

Table 3

Chemicals and target phases of the sequential Fe extraction procedure, which consists of a combination of extraction steps presented in Poulton and Canfield (2005) and Claff et al. (2010).

Extractant (extraction time)	Target phase	Term	Reference
1 mol L^{-1} HCl, pH 0 (4 h)	Poorly ordered or acid-soluble Fe(II) and Fe(III) minerals (ferrihydrite, Fe carbonate, Fe monosulfide)	HCl-Fe(II) and HCl-Fe (III)	Claff (2010)
0.35 mol L^{-1} acetic acid/0.2 mol L^{-1} Na_3-citrate/50 g L^{-1} Na dithionite, pH 4.8 (4 h)	Crystalline oxide minerals (goethite, hematite)	CBD-Fe; crystalline Fe(III)[b]	Poulton (2005), Claff (2010)
0.17 mol L^{-1} NH_4 oxalate/0.2 mol L^{-1} oxalic acid, pH 3.2 (6 h)	Recalcitrant oxide minerals (magnetite) [a]	oxalate-Fe[a]; crystalline Fe(III)[b]	Poulton (2005)
65% HNO_3 (2 h)	Pyrite[c]	FeS_2-Fe	Claff (2010)

[a] Due to likely partial dissolution of magnetite in 1 M HCl (Poulton and Canfield 2005) and the acetic acid-citrate-dithionite solution (Claff et al. 2010), this likely only represents the most recalcitrant magnetite.

[b] In light of the above uncertainty, CBD-Fe and oxalate-Fe are collectively referred to as crystalline Fe(III) (ox-Fe).

[c] This extraction step may dissolve small amounts of clay-associated Fe and thereby overestimate the concentration of pyrite-Fe (Lord 1982).

Table 4

Chemicals and target phases of the sequential P extraction procedure, a streamlined version of the SEDEX procedure of Ruttenberg (1992), with all H_2O wash steps and selected $MgCl_2$ steps removed (Slomp et al. 1996).

Extractant (extraction time)	Target phase	Term
1 mol L^{-1} $MgCl_2$ brought to pH 8 (0.5 h)	Exchangeable P	exch-P
0.3 mol L^{-1} Na_3 citrate/1 mol L^{-1} $NaHCO_3$/25 g L^{-1} Na dithionite, pH 7.6 (8 h)[a]	P bound to easily reducible Fe(III) (oxyhydr)oxides, vivianite[b] (Fe (II)$_3$(PO$_4$)$_2$·8H$_2$O)	CDB-P
1 mol L^{-1} Na acetate buffered to pH 4 with CH_3COOH (6 h)[a]	Carbonate fluorapatite, hydroxyapatite	acetate-P
1 mol L^{-1} HCl (24 h)	P in detrital minerals	HCl-P
1 mol L^{-1} HCl (24 h), after ashing at 550 °C	P in organic matter	organic P

[a] Followed by 1 mol L^{-1} $MgCl_2$ (adjusted to pH 8 with NaOH) wash step to extract P that was resorbed during extraction.

[b] Potential for vivianite dissolution in this solution shown by Nembrini et al. (1983) and Dijkstra et al. (2014).
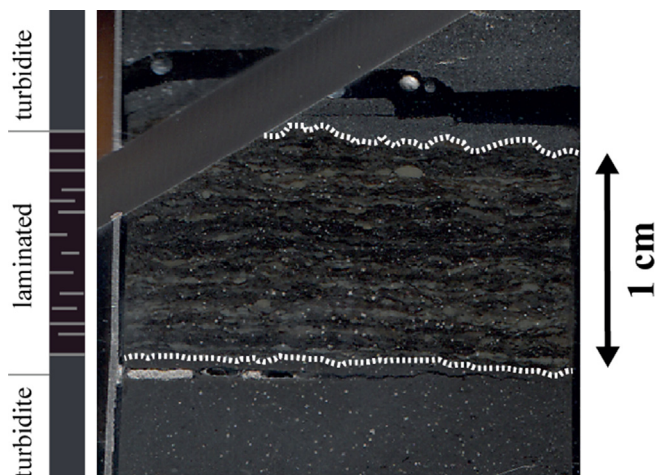
Fig. 2. Selected depth interval (29–31 cm core depth) of the polished resin-impregnated core from station 1, showing an alternation of homogenous turbidite layers (bottom and top) and mm-scale laminated marine sediment (middle) with the latter being characteristic of regular deep Black Sea sedimentation. White dashed lines highlight the bottom and top of the laminated interval. The white dots seen in the image are visual artifacts of the polishing process and subsequent scanning of the resin block and do not represent sedimentary features.

and Fe and depleted in $CaCO_3$ and C_{org} relative to normal marine sediment (Fig. 3i, j, k, l). This correspondence was not observed at greater sediment depth, where the chemical signature of the thin normal marine intervals was not detected due to the relatively low sampling resolution. The high Al and Fe contents of the turbidite intervals results from the stronger terrestrial signature of the source material compared to deep basin sedimentation where terrestrial components are diluted by biogenic $CaCO_3$. The Al-normalized profiles at station 1 show a relatively constant Fe concentration throughout the core and clear S enrichments in the normal marine intervals. Phosphorus and molybdenum concentrations show enrichments in the normal marine intervals both in the bulk and Al-normalized profiles.

The vertical solid-phase profiles from SW slope station 13 (234 mbss) showed relatively little variability apart from various Mn peaks (Fig. 3e). The Al, C_{org}, $CaCO_3$ and Fe contents in the SW shelf sediments (Fig. 3a, b, c, d) were very similar to those observed in the turbidite intervals from the SW deep station. The SW slope sediments contained relatively high concentrations of Mn and P and, by contrast, relatively low concentrations of S and Mo compared to SW deep sediments.

3.2. Bulk pore-water geochemistry and micro-profiles

Dissolved Si showed a relatively high variability at the SW slope station 13, with a strong increase from the bottom water to the uppermost sediment sample at 2 cm depth (Fig. 4a). Dissolved SO_4^{2-} decreased down-core at both stations, with a rapid decrease from sea-water values to SO_4^{2-} below detection in the top 27 cm of sediment at station 13 (Fig. 4b). Here, dissolved CH_4 reached concentrations up to ~ 0.5 mmol L^{-1}, with a sulfate-methane transition zone (SMTZ) at around 15–25 cm sediment depth (Fig. 4b). Pore-water HS^- concentrations up to 1.1 mmol L^{-1} were observed at station 1, while no free HS^- was detected throughout the core from station 13 (Fig. 4c, k). At station 13, the DIC concentration showed a down-core increase from 8 to 38 mmol L^{-1} that was much stronger than that at deep station 1, where DIC did not exceed 9 mmol L^{-1} (Fig. 4d, l). The highest NH_4^+ accumulation with values up to 485 μmol L^{-1} was observed at the deep site (Fig. 4e, m). Dissolved PO_4^{3-}, Fe^{2+} and Mn^{2+} were relatively low in the core from station 1: Fe^{2+} and Mn^{2+} were < 5 μmol L^{-1} and PO_4^{3-} did not reach beyond ~ 30 μmol L^{-1} (Fig. 4n, o, p). By contrast, station 13 sediment showed strong sub-surface accumulations of PO_4^{3-}, Fe^{2+} and Mn^{2+} to high concentrations generally > 200 μmol L^{-1} with large variability (Fig. 4f, g, h). The rapid accumulation of Fe^{2+} started at a slightly greater depth than Mn^{2+}, and dissolved PO_4^{3-} and Fe^{2+} showed mirror-image profiles.

Analysis of the discrete sediment samples from station 13 did not reveal detectable sulfide (Fig. 4c), but the voltammetric micro-profiling revealed accumulation of ΣH_2S (H_2S, HS^- and $FeS_{(aq)}$) up to 100 μmol L^{-1} in the uppermost sediment, with a subsequent decrease to values below detection between 0.5 and 4 cm sediment depth (Fig. 5a). We attribute the lack of this surface enrichment in the results from the discrete samples to a much lower sampling resolution (cm-scale rather than sub-mm scale) and possible loss of sulfide during sampling and pore-water extraction. The voltammetric sulfide signals showed a ratio < 1 between the height of the forward sulfide peak (sensitive to HS^-/H_2S only) and the height of the reverse wave (sensitive to both HS^-/H_2S and aqueous FeS). This indicates that most of the sulfide determined by voltammetry at station 13 was not in the form of HS^-/H_2S, but occurred as aqueous FeS clusters/nanoparticles (Luther III et al. 2001; Luther III and Rickard 2005). This pointed to the accumulation of dissolved Fe–S phases in the surface sediment from metal-rich station 13. No dissolved Fe^{2+} was detected at station 13 with voltammetry, but dissolved Mn^{2+} accumulated downcore to concentrations up to 1600 μmol L^{-1} (Fig. 5a). By contrast, in the discrete pore-water samples, Fe^{2+} and Mn^{2+} reached concentrations of up to ~ 1 mmol L^{-1} and 0.5 mmol L^{-1}, respectively (Fig. 4g, h). It is probable that the Fe voltammetric signal was masked by the Mn signal around −1.6 V. As both solutes increased in concentration, the wave-like Fe and Mn signals could overlap thereby jointly contributing to the Mn signal.

For station 1, the voltammetric data showed the down-core accumulation of dissolved HS^- up to ~ 700 μmol L^{-1}, with up to ~ 1000 μmol L^{-1} HS^- measured in the discrete samples (Fig. 5b).
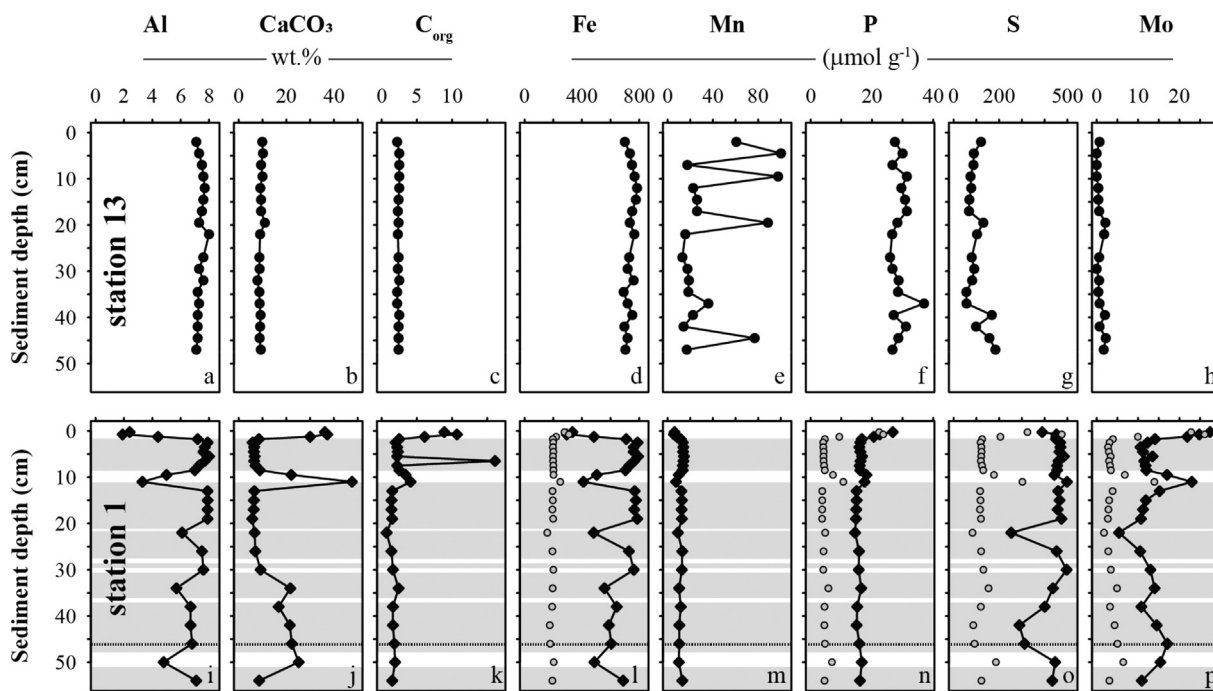
Fig. 3. Profiles of key solid-phase species for stations 13 (234 mbss) and 1 (2169 mbss). Grey zones indicate turbidite intervals at station 1, based on visual observation of homogeneous grey material alternating with thin intervals of laminated normal marine sediment. Small grey symbols in panels for Fe, P, S and Mo at station 1 show Al-normalized profiles ($2 \times$ element/Al, µmol/wt%). Black horizontal arrows in panel 3 g indicate S enrichments associated with sulfide production and enhanced S sequestration (see section 4.2). Dashed horizontal line indicates depth below which no resin-embedded sediment was available and thus no visual identification of turbidite or marine intervals was possible. Note that below 20 cm core depth, the resolution of discrete sampling for chemical analysis of sediment was 4 cm per section while the intervals of normal marine sedimentation were ~1 cm. As a result, sediment composition no longer reliably reflects differences in sediment type (normal marine versus turbidite).
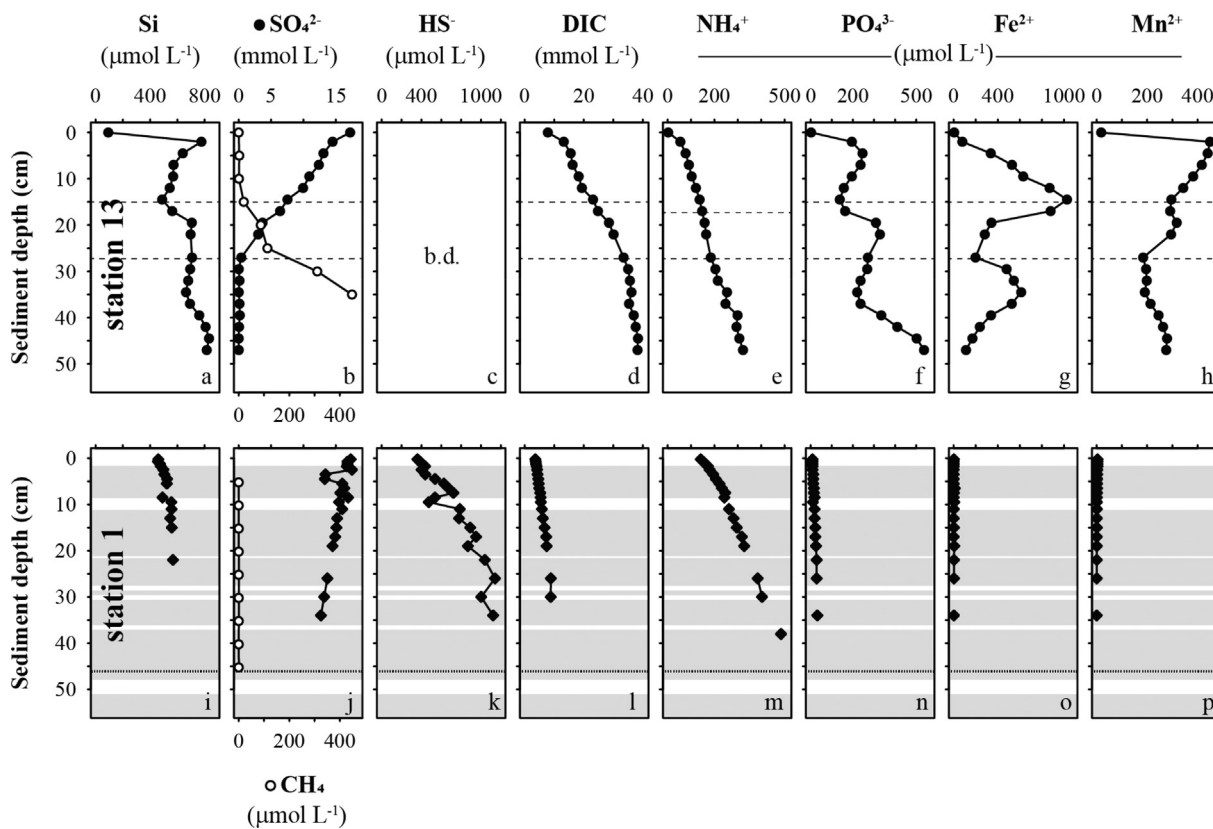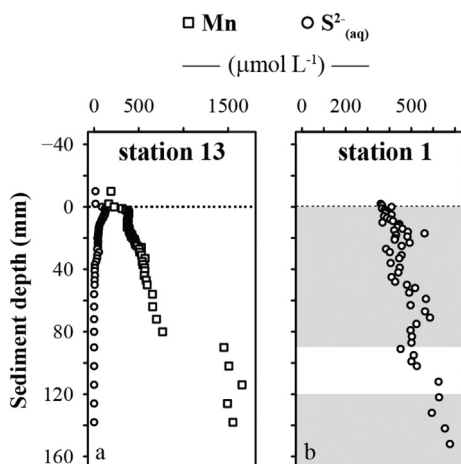

Fig. 4. Profiles of key pore-water species for stations 13 (234 mbss) and 1 (mbss). Sulfide for station 13 (Fig. 4c) was below the practical detection limit (~ $1 \, \mu mol \, L^{-1}$). Grey zones indicate turbidite intervals at station 1 as described in caption of Fig. 3. Dashed horizontal line indicates SMTZ as interval between first appearance of CH_4 and depletion of SO_4^{2-}.

Fig. 5. Micro-electrode profiles of key reduced pore-water species (Mn^{2+}, HS^-) for stations 13 and 1. Note that no dissolved Fe^{2+} was detected by voltammetry at either station; in the case of station 13 this was likely caused by masking of the Fe voltammetric signal by the Mn signal (see section 3.2). Note the mm-scale y-axis, with negative numbers for depths above the sediment-water interface (dashed horizontal line). Grey zones indicate turbidite intervals at station 1 as described in the caption of Fig. 3.

3.3. Sediment iron and phosphorus pools

The sediments from SW slope station 13 showed relatively high dissolved Fe^{2+} concentrations and abundant reactive solid-phase Fe phases in the form of poorly ordered and crystalline ferric Fe (HCl-Fe (III), ox-Fe) and labile ferrous Fe, HCl-Fe(II) (Fig. 6a – i). HCl-Fe(III) showed an overall downward decrease with two distinct peaks that co-occurred with maxima in dissolved Fe^{2+}. Pyrite (FeS_2-Fe) was not an important Fe phase in the SW slope sediments. The DOP was low (< 0.2) throughout the station 13 sediment core, with a subsurface peak at ~ 2 cm depth. Ferric Fe was abundant throughout the core and made up 50 ± 10% (*n* = 18) of highly reactive Fe, which in turn accounted for 48 ± 1% of the total Fe pool. The Fe/Al ratio (wt% wt

$\%^{-1}$) was stable at 0.56 ± 0.01.

The iron chemistry of the deep station 1 sediments reflects a strongly reducing character (Fig. 6i – r). HCl-Fe(III) was very low throughout the core, and the ox-Fe pool was much smaller than in the slope sediments. HCl-Fe(II) made up ~ 20% of highly reactive Fe at the SW deep station 1 with enrichments up to 95 $\mu mol\,g^{-1}$ in the turbidite intervals. FeS_2-Fe was the dominant Fe pool, the DOP ranged between 0.6 and 0.8. The highly reactive Fe pool represented 50 ± 8% of total Fe with higher values in the normal marine sediment intervals; the Fe_{HR}/Fe_{tot} ratio in the turbidite intervals was very similar to that of station 13. A similar pattern was observed for the Fe/Al ratio: generally elevated values in the normal marine intervals and values similar to those at station 13 for the turbidite intervals.

Total solid-phase P was generally higher in the sediments from slope station 13 (29 ± 3 $\mu mol\,g^{-1}$) compared to deep basin station 1 (17 ± 3 $\mu mol\,g^{-1}$) (Fig. 7b, j). The surface enrichment in P at station 1 was attributable to CDB-P and org-P (Fig. 7j, n, p). At station 1, org-P showed an overall decrease with sediment depth while Ca−P and, to a lesser extent, det-P increase down-core (Fig. 7c, d, e). The Ca−P record shows clear enrichments in the turbidite intervals in the top 20 cm. The normal marine intervals in the top 10 cm record enrichments in CDB-P and, to a lesser extent, CDB−Mn, whereas CDB-Fe is relatively depleted (Fig. 7n, o, p). Station 13 showed rather constant concentrations of tot-P (Fig. 7b), org-P (Fig. 7c) and Ca−P (Fig. 7d) throughout the core, while det-P (Fig. 7e) increased down-core. The CDB−P, CDB-Fe and CDB-Mn concentrations at station 13 (Fig. 7f, g, h) were all markedly higher than at station 1. The CDB-extractable Fe, Mn and P all showed relatively high variability and a pronounced decrease between 20 and 35 cm sediment depth. In addition, CDB-Fe at station 13 showed a general down-core decrease.

4. Discussion

4.1. Sediment geochemistry in the western Black Sea – Spatial variability in the relative contribution of terrigenous and biogenic materials

Combining our current findings and results from previous work (Kraal et al. 2017), we can compare slope and deep stations from the
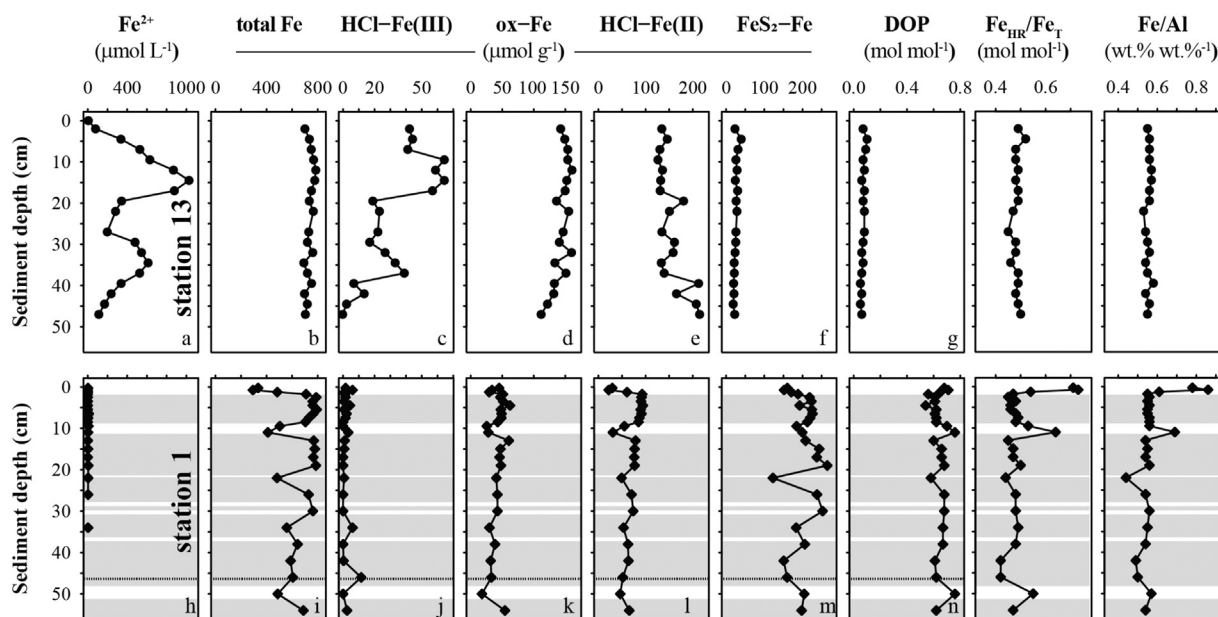
Fig. 6. Dissolved Fe^{2+} and solid-phase Fe species as determined by sequential chemical extraction: total Fe; 1 M HCl-soluble ferric Fe (HCl-Fe(III)); ferric Fe in crystalline (oxyhydr)oxides (ox-Fe); 1 M HCl-soluble ferrous Fe (HCl-Fe(II)), Fe in pyrite (FeS_2-Fe). Panel on the right shows degree of pyritization (DOP), calculated as the fraction of the highly reactive Fe present as FeS_2-Fe. For methodological details, see section 2.5. Grey zones indicate turbidite intervals at station 1 as described in caption of Fig. 3.
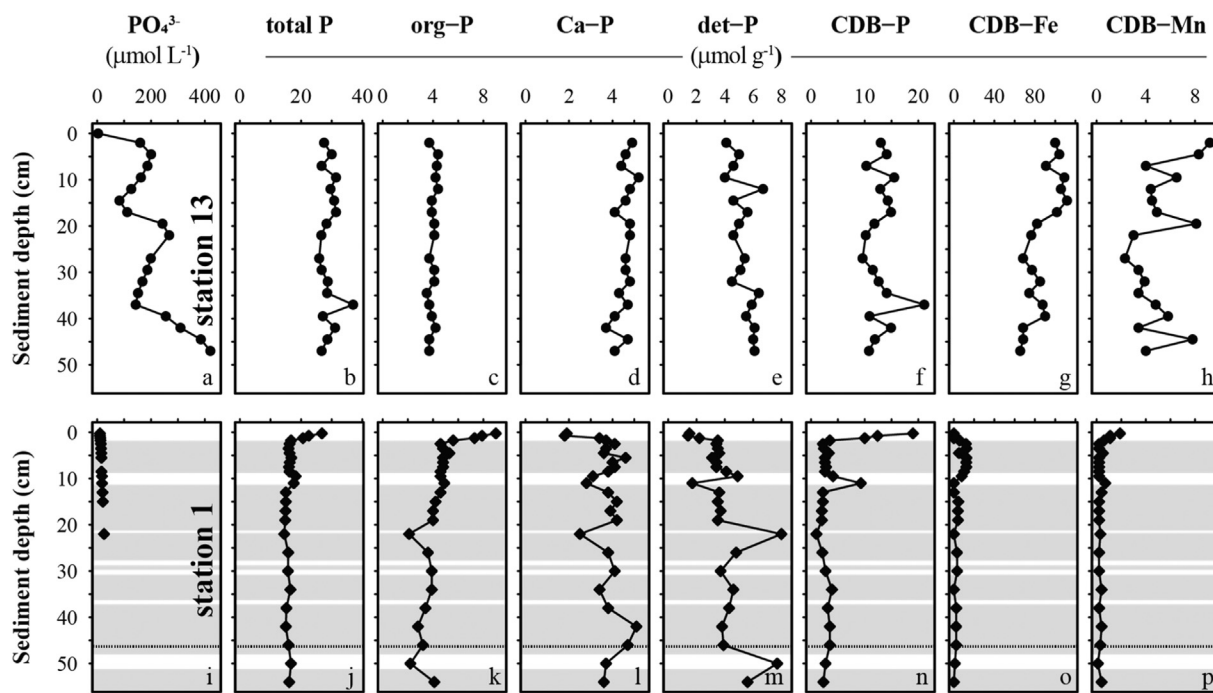
Fig. 7. Dissolved PO_4^{3-} and solid-phase P species as determined by sequential chemical extraction: total P; organic P (org-P); P in authigenic calcium phosphate minerals (Ca−P); P in detrital minerals (det-P), P associated with easily reducible Fe (and Mn) (oxyhydr)oxides (CDB−P). Two panels on the right show Fe and Mn extracted during CDB-P extraction. For methodological details, see Section 2.5. Grey zones indicate turbidite intervals at station 1 as described in caption of Fig. 3.

northern (6A, 120 mbss and 2, 2107 mbss) and southern (13, 234 mbss and 1, 2169 mbss) regions of the western Black Sea (Table 1, Fig. 1). In contrast to station 1, station 2 in the deep Black Sea showed no signs of turbidites in the 36-cm surface sediment record investigated by Kraal et al. (2017).

The sediments from the SW Black Sea stations that were sampled relatively close to the Bosporus inflow have a stronger terrestrial signature than their NW counterparts, as evidenced by higher Al and Fe content (Fig. 8a, b). Similar high Fe concentrations were found in terrigenous sediments from more shallow water depths (< 100 mbss) close to the Danube inflow on the NW shelf (Wijsman et al. 2001; Lenstra et al. 2018). A strong terrestrial signature at the SW slope station 13 is also in line with previous findings at a slightly deeper station on the slope near the Bosporus inflow, where surface sediments were

described as black terrigenous silts (station BS 98-18 at 485 mbss in: Oaie et al. 2005). The low Al content at deep NW station 2 reflects regular deep Black Sea sedimentation with relatively little terrestrial input away from the shelf, while turbidite deposition has resulted in a relatively high abundance of and variability in sedimentary Al content at deep SW station 1.

The Mn and P concentrations at the investigated stations varied in relation to water depth rather than geographic area, with highest concentrations in the NW and SW slope sediments that were overlain with oxygenated bottom waters (Fig. 8c, d). The S concentrations showed an opposite trend with depth (Fig. 8g): highest S concentrations were measured in the sediments from the deep stations where strongly sulfidic bottom and pore-waters drive Fe sulfidation and pyrite enrichment. The degree of Fe sulfidation (DOP) is high at all stations
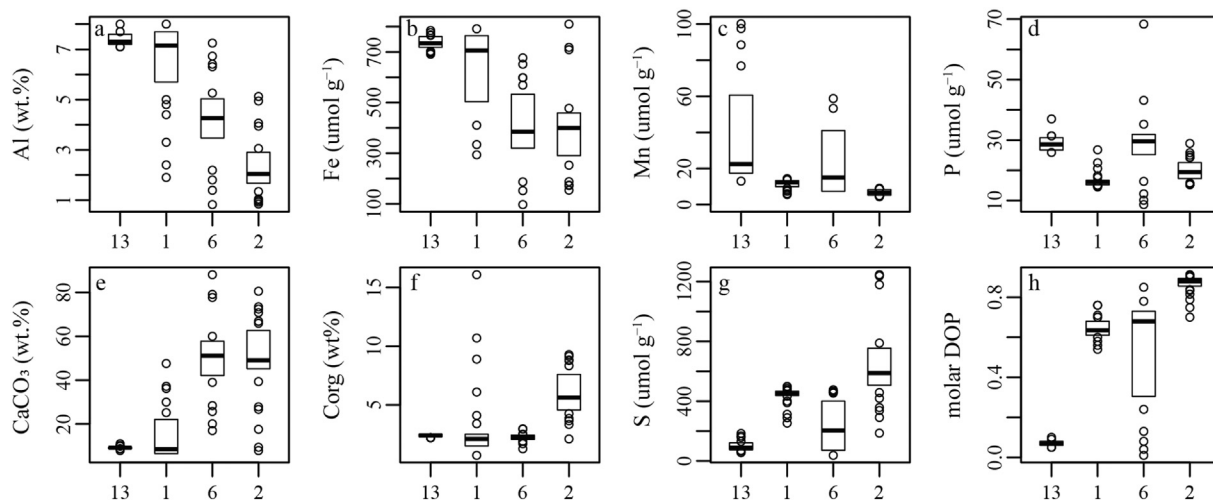

Fig. 8. Box and whisker plots for key solid-phase species for stations 1, 5, 6A and 13. Two extreme values for station 6A (204 and 714 μmol g^{-1}) were omitted from the figure, but not from the calculation of the average and percentiles. Upper and lower limit of box represents third and first quartile, respectively, and the horizontal thick line in box represents median. Open circles represent data points outside the box range.

except station 13, where only a small fraction of the abundant reactive Fe is sulfidized (see Section 4.2).

High C_{org} concentrations are mostly restricted to the deep basin, in particular station 2, magnified by decreased dilution of C_{org} by terrigenous sedimentation and slow OM turnover under anoxic and sulfidic conditions (Fig. 8f). Station 1 shows high C_{org} contents for the normal deep marine sediment intervals (see also Fig. 3k), but overall rather low C_{org} content due to the dominant impact of the relatively C_{org}-poor turbidite intervals.

There is a stark contrast in sedimentary $CaCO_3$ contents between the NW and SW stations (Fig. 8e). The NW slope station 6A showed several dense bivalve shell beds ($CaCO_3$) in the investigated sediment record, while the sediment at SW slope station 13 consisted of terrigenous silts. Deep station 1, with abundant turbidite intervals, has much lower $CaCO_3$ contents than deep station 2 that is characterized by normal marine sedimentation. Additionally, the NW area is located closer to the inflow of the major rivers that discharge nutrients into the Black Sea, which can drive higher primary productivity and thus biogenic calcium carbonate input in the NW area (Tolmazin 1985b; Grégoire et al. 1998; Strokal and Kroeze 2013). In comparison, nutrient input on the SW shelf and slope by inflow of Mediterranean waters from the Sea of Marmara through the Bosporus Straight is limited (Tolmazin 1985a; Tugrul et al., 2002). The relatively high accumulation rates of (terrigenous) material in the SW Black Sea (Teodoru et al. 2007; Yücel et al. 2012) further act to dilute the biogenic sediment component and enhance the terrestrial signature of these sediments.

4.2. Sediment geochemistry on the southwestern Black Sea slope (station 13)

The rapid down-core SO_4^{2-} depletion and CH_4 accumulation on the SW slope suggests high biogeochemical activity. In addition, there is input of Fe and Mn species (likely (oxyhydr)oxides) that are rapidly reduced resulting in large stores of dissolved Fe^{2+} and Mn^{2+} and highly reactive, solid-phase Mn and ferrous and ferric Fe phases (Fig. 6c, d, e), in comparison to both the deep SW station 1 and the shelf, slope and deep stations in the NW Black Sea (Kraal et al. 2017). Similar strong enrichments in solid-phase Fe and dissolved Fe^{2+} and Mn^{2+} have been found previously in SW slope sediments (Konovalov et al. 2007).

The SO_4^{2-} profile from station 13 is characterized by two trends: an exponential decrease in the top $\sim$ 10 cm, and a linear decrease below this depth down to the sulfate-depleted sediment in the SMTZ. The former is characteristic for dissimilatory microbial SO_4^{2-} reduction coupled to OM oxidation, the rate of which generally rapidly decreases with sediment depth. The latter reflects diffusive transport of SO_4^{2-} into the SMTZ, where it is consumed during anoxic oxidation of methane (AOM):

$$CH_4 + SO_4^{2-} \rightarrow HS^- + HCO_3^- + H_2O \tag{1}$$
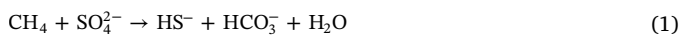
The pore-water profiles suggest that SO_4^{2-} depletion below 10 cm sediment depth is mostly due to AOM. This observation is supported by the modest down-core increase in NH_4^+ in combination with strong DIC (HCO_3^-) accumulation (Fig. 4d). If sulfate reduction coupled to OM degradation was responsible for SO_4^{2-} removal below 10 cm sediment depth, the release of OM-associated N (assuming Redfield's C/N of 16) would have resulted in NH_4^+ an order of magnitude higher than measured (Fig. 4e) (Burdige and Komada 2013). The stoichiometric mismatch between SO_4^{2-} (up to 17 mmol L^{-1}) and CH_4 (up to 0.5 mmol L^{-1}) that react in a 1:1 ratio (Eq. 1) in AOM (Eq. (1)) is likely attributable to extensive CH_4 loss by outgassing during sampling (Egger et al. 2016).

The production of sulfide in two distinct zones (surface sediment and SMTZ) by separate processes is also reflected in the solid-phase S profile that shows subtle enrichments in both intervals (Fig. 3g). In addition, the minima in Fe(III) in the surface and SMTZ sediments point

towards sulfide-driven reduction and transformation of highly reactive ferric Fe in these sediment intervals (Fig. 6). In the surface sediment, voltammetric measurements revealed the presence of up to 100 μmol L^{-1} "dissolved" sulfide, likely in the form of $FeS_{(aq)}$ (Fig. 5a). This suggests that microbially produced sulfide in these metal-rich sediments is present in nano-particulate clusters rather than free dissolved HS^-. Nano-scale FeS complexes thus may play an important but at present still poorly constrained role in Fe dynamics in reducing sediments.

Against a setting of rapid conversion of SO_4^{2-} to HS^- in station 13 sediment, the lack of solid-phase S accumulation is striking. We can approximate SO_4^{2-} removal rates in the top sediment and the SMTZ by representing them as diffusive fluxes:

$$J_{SO4} = -\varphi \times D_{SO4,sed} \times \frac{dC}{dz} \tag{2}$$

where J_{SO4} represents the flux of SO_4^{2-} (μmol cm^{-2} s^{-1}), φ represents porosity (cm^3 cm^{-3}, assumed 0.8), $D_{SO4,\ sed}$ represents the diffusion coefficient of SO_4^{2-} in the sediment (Boudreau 1997) and $\frac{dC}{dz}$ represents the concentration gradient in the surface sediment (0–2 cm) or around the SMTZ (10–25 cm). For sulfide production by microbial dissimilatory sulfate reduction (DSR) in the surface sediment and AOM around the SMTZ, we obtain rates of $\sim$600 and 150 μmol cm^{-2} y^{-1}, respectively. Corrected for vertical extent (2 cm for the surface sediment, 5 cm for the SMTZ based on the S enrichment in Fig. 3) and dry bulk density, and assuming that all S produced is sequestered in the sediment, we obtain S accumulation rates of $\sim$ 380 and 35 μmol g^{-1} y^{-1} in the surface sediment and SMTZ, respectively. These high rates contrast with the relatively low solid-phase S content of 99 $\pm$ 38 μmol g^{-1}. This would require sedimentation rates of several cm per year, which would be exceptionally high for non-turbidite Black Sea sediments (Konuk et al. 1991; Crusius and Anderson 1992). We instead propose that periodic reworking of the mobile muds on the SW slope, possibly related to the same mass movement processes that drive turbidity currents, may help explain this mismatch between pore-water chemistry (high sulfide production) and sediment composition (low sulfide) that is in fact typical for non-steady state diagenesis (Aller 1998). Additionally, previous experimental data and modelling results from reducing sediments on the Namibian shelf indicate that efficient microbial sulfide oxidation to sulfate can result in very low sedimentary sulfide concentrations despite high rates of DSR (Dale et al. 2009).

While DSR and sulfide production clearly affect Fe redox chemistry, there is a strong excess of highly reactive solid-phase Fe(II) and Fe(III) (Fig. 6c, d, e) over S and DOP (Fig. 6g) is low. Iron monosulfide (FeS) was not measured but can be approximated as the difference between total S and the sum of pyrite-S and seawater-derived S (SO_4^{2-}) that remained in the sediment after freeze-drying. The latter was estimated from the measured salinity of 21 and an assumed porosity of 0.8. It is likely that FeS is overestimated because the calculation disregards elemental sulfur, a common sediment S pool in sediments where sulfide reacts with oxidants such as O_2 and Fe(III) (Rickard and Luther 2007). The FeS shows a peak in the SMTZ and a strong downward increase below $\sim$ 35 cm sediment depth (Fig. 9). Concurrent peaks are observed in the fraction of sulfidized Fe, represented by FeS as fraction of HCl-Fe (II) (Fig. 9e) and by total sulfidized Fe as fraction of Fe_{HR} (Fig. 9f). Nonetheless, sulfidized Fe on average makes up only $\sim$ 20% of the highly reactive Fe pool at station 13 and this SW slope sediment retains abundant ferrous and ferric Fe phases that are reactive towards sulfide.

Some insight into the nature of these Fe phases may be gained by looking at other dissolved species. The abundance of dissolved Fe^{2+}, PO_4^{3-} and DIC at slope station 13 would facilitate precipitation of Fe (II) phosphate (e.g. vivianite) or Fe(II) carbonate (e.g. siderite) as ferrous Fe phases that are reactive towards sulfide (McAnena 2011; Dijkstra et al. 2018a), represented by Fe(II)$_{nonsulf}$ in Fig. 9d. Chemical modelling with Visual MINTEQ showed that pore-waters at station 13 are supersaturated with respect to both. Importantly, our results show a
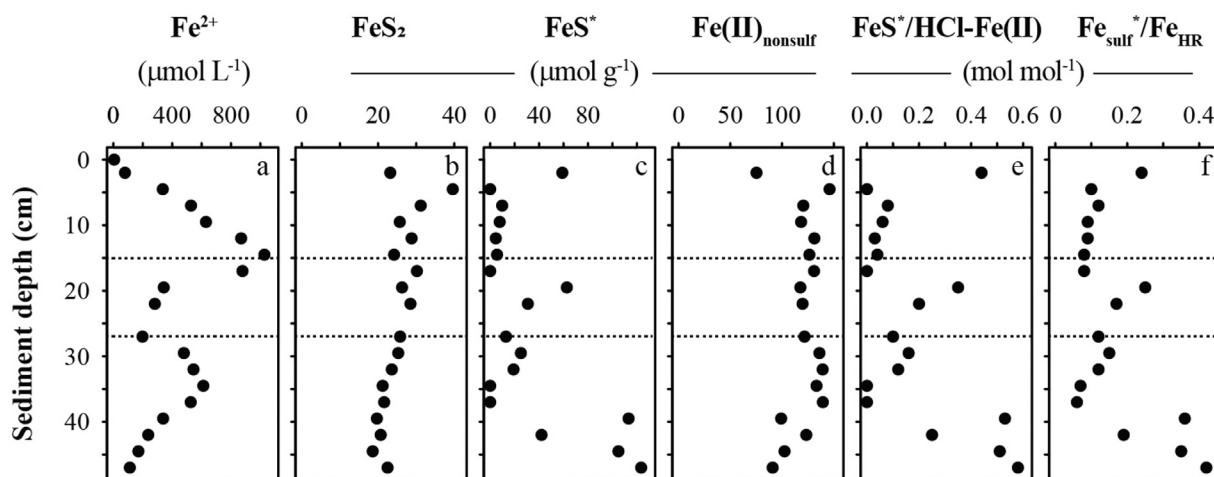
Fig. 9. Profiles of measured and calculated (indicated with asterisk, *) iron species for station 13. Also included are the following ratios for Fe sulfidation: FeS as fraction of 1 M HCl-extractable Fe(II) (panel e), and total sulfidized Fe (Fe$_{sulf}$, which is FeS* + pyr-Fe) as fraction of highly reactive Fe (panel f). The latter ratio is in fact the degree of Fe sulfidation (DOS) sensu Boesen and Postma (1988). Dashed horizontal lines indicate the approximate upper and lower boundary of the sulfate-methane transition zone.

relatively large sulfide buffering capacity in the anoxic sediments from the SW Black Sea slope. These sediments contain significantly higher concentrations ($> 300\,\mu mol\,g^{-1}$) of highly reactive, non-sulfidized Fe phases at depth compared to the north-west Black Sea slope with $< 100\,\mu mol\,g^{-1}$ of crystalline Fe (oxyhydr)oxides below the oxic uppermost surface sediment (Kraal et al. 2017). Lastly, the profiles of solid-phase Fe species at station 13 with (transient) minima in Fe(III) (Fig. 6c) and peaks in sulfidized Fe(II) (Fig. 9b, c) further emphasize the aforementioned notion that the processes controlling Fe redox chemistry at station 13 are not at steady state.

4.3. The impact of turbidity currents on Black Sea Fe–S cycling

4.3.1. Changes in Fe chemistry during turbidite transport, deposition and burial

The southwest margin of the Black Sea is seismically very active with frequent earthquake-related mass movement events (Konuk et al. 1991; Konovalov et al. 2007; Yücel et al. 2010b). Our work adds to existing knowledge on the turbidite distribution and geochemistry of sediments in the deep Black Sea. If we assume that the slope sediment at station 13 is representative for material that is entrained in turbidity currents and deposited in the deep SW Black Sea, we can use this to assess the geochemical impact of introducing such sediment into the sulfidic deep Black Sea. While speculative, comparison of geochemical records lends credibility to this assumption. Firstly, the bulk chemistry (CaCO$_3$, Al, Fe) of the slope sediment (Fig. 3a, b, d) is very similar to that of buried turbidite intervals at station 1 (Fig. 3i, j, l) that is located downslope, approximately 60 km to the northeast, of station 13. Secondly, the crystalline Fe oxide content in station 13 sediment ($138 \pm 13\,\mu mol\,g^{-1}$) is very similar to dithionite-extractable Fe (i.e. labile and crystalline Fe oxides) in a very recent turbidite deposited some 200 km to the northeast (station 8–30 in (Yücel et al. 2010a)) (Fig. 1). These observations support the notion that deposition of turbidites with an original geochemical composition similar to that of the investigated slope sediments at station 13 is widespread in the SW Black Sea.

The potential of turbidity currents to affect geochemical cycling in the Black Sea was explored previously. Yücel et al. (2010a, 2010b) reported a 20 cm-thick, Fe oxide-rich turbidite interval in the western Black Sea, sourced from shallower depths in the SW Black Sea and transported into the deep sea during a 1999 earthquake. The turbidite interval was deposited on top of normal micro-laminated and sulfide-rich deep Black Sea sediment and was itself covered by 2 cm of fluffy

surface sediment. The HS$^-$ concentrations in the turbidite interval were lower than in surrounding layers and an anomalous accumulation of zero-valent sulfur, a product of sulfide oxidation, was also observed. The authors applied a reactive-transport model to reconstruct sediment diagenesis after deposition, assuming an initial highly reactive, non-sulfidized Fe pool of $80\,\mu mol\,g^{-1}$ Fe oxide in the form of the crystalline (oxyhydr)oxide goethite. The model results showed that the introduction of such a Fe(III) pool could contribute significantly to S cycling (HS$^-$ oxidation and pyrite formation) in deep Black Sea sediments. Our results, with detailed geochemical characterization of deep Black Sea turbidite intervals and of sediment from a turbidity current source area, allow us to further explore the impact of turbidite inputs on geochemical cycling in the Black Sea.

Firstly, we note that the content of Fe phases that are potentially reactive towards HS$^-$ can be much higher than assumed in the turbidite diagenesis model by Yücel et al. (2010b). In the model, $80\,\mu mol\,g^{-1}$ of crystalline Fe(III) (goethite) was assumed, while the actual turbidite interval on which the model was based contained $100–150\,\mu mol\,g^{-1}$ dithionite-extractable Fe (Yücel et al. 2010a). We show that crystalline Fe(III) is only a part of the total pool Fe that is reactive towards HS$^-$ and can be transported into the sulfidic deep Black Sea by turbidity currents. In addition to crystalline Fe(III) oxides, the source sediment at station 13 also contains $187 \pm 16\,\mu mol\,g^{-1}$ of 1 M HCl-extractable Fe (i.e. labile, Fe(II)/Fe(III)) that is assumed to be highly reactive towards HS$^-$ on timescales of seconds to days (Canfield et al. 1992; Poulton et al. 2004). As such, HS$^-$ oxidation and FeS$_2$ formation by reaction of native HS$^-$ with allochthonous Fe(II) and Fe(III) may be quantitatively much more important than previously assumed.

Our record with detailed chemical characterization of recurring turbidite intervals alternating with thin layers of normal deep Black Sea sediment offers a unique opportunity to explore the diagenetic fate of the different Fe phases. In the reactive-transport model of turbidite diagenesis of Yücel et al. (2010b), all reactive Fe (goethite) in a 20-cm thick turbidite is transformed into the stable end-member pyrite, FeS$_2$, within 20 years after turbidite deposition. Our results, by contrast, show variable responses of the different Fe phases to transport and deposition under sulfidic conditions. The HCl-Fe(III) pool, which already disappears at depth in the anoxic sediment at slope station 13, is absent in the sulfidic sediment at station 1 (Fig. 6). The labile ferric Fe is likely reduced and sulfidized during water column transport or at the sediment surface in the deep basin. By contrast, significant amounts of crystalline Fe oxides and HCl-Fe(II) are present throughout the sediment record at station 1. Comparison of station 13 surface sediment to

the most recent turbidite interval at station 1 (3–8 cm depth) shows a decrease of ~65% in ox-Fe and a decrease of ~30% in HCl-Fe(II). Both of these Fe pools are enriched in the turbidite intervals and only a gradual decrease of ~50% occurs with depth in the sediment at station 1.

Providing age estimates for the sediment record at station 1 is challenging. Visual observations showed erosional features associated with the deposition of turbidite intervals, and mixing of normal marine sediment and turbidite material. It is therefore likely that intervals of normal marine sedimentation are underestimated. We assume instantaneous deposition of turbidites and sedimentation rates of 0.2 to 0.02 cm y^{-1} for newly deposited and compacted deep Black Sea sediments, respectively (Anderson and Raiswell 2004; Dijkstra et al. 2018b). We use 0.1 cm y^{-1} as an average sedimentation rate because of the uncertainty regarding the degree of compaction for the various sediment intervals. The uppermost turbidite (2–8 cm) was overlain by ~ 2 cm of undisturbed fresh sediment (and fluff layer) and accordingly has an estimated age of ~ 20 y. The second turbidite (12–22 cm) is overlain by ~3 cm of compacted sediment and thus was likely deposited at least 50 y ago. Below this, the thickness of the normal sediment intervals is hard to ascertain, but these deeper turbidites are likely decades older still.

Despite their inherent uncertainty, these age estimates illustrate that highly reactive Fe phases can survive under strongly reducing conditions much longer than expected. It is possible that sulfidation of Fe mineral surfaces effectively protects particles from further sulfidation (Canfield et al. 1992). The slightly variable but downward-increasing HS$^-$ profile at station 1 (Fig. 4k) contrasts with the strong sulfide depletion observed in reactive Fe-rich turbidite interval by Yücel et al. (2010a), and further illustrates the low reactivity of these Fe phases towards sulfide. Lyons and Berner (1992) found similarly low reactivity towards sulfide of deep Black Sea turbidite material and hypothesized a fundamentally different, less reactive, character of the turbidite material compared to normal deep Black Sea sedimentation. Overall, we show that the total reactive Fe reservoir in turbidity currents that may contribute to HS$^-$ oxidation and pyrite formation may be larger than previously assumed, and that the timescales on which the Fe phases react with sulfide differ markedly. As such, turbidity currents in the Black Sea can have a significant and long-lasting impact on Fe–S geochemical cycling in the basin.

4.3.2. Quantitative assessment of turbidite-associated iron and sulfur fluxes

To assess the quantitative importance of turbidite deposition, we perform some simple calculations using the uppermost turbidite interval as this was overlain by undisturbed surface sediment and thus likely suffers the least from the above-described age uncertainties. The turbidite interval is ~8 cm thick, and the turbidite and overlying sediment together represent ~ 20 years of sedimentation. We use an estimate for the deep (> 1800 mbss) SW Black Sea of 20,000 km^2 (total abyssal area 170,500 km^2; (Teodoru et al. 2007)) (Table 5). The data from station 13 surface sediments show ~ 300 µmol g^{-1} of highly

Table 5
Parameters used to estimate contribution of turbidite deposition to Black Sea Fe fluxes. "P loss from sediment" is calculated as the difference in the average sediment P concentration between station 13 and station 1 (Fig. 3f, n).

Parameter	Estimate	Source
Area deep Black Sea (> 1800 mbss)	170,500 km^2	Teodoru et al. (2007)
Area deep SW Black Sea	20,000 km^2	Teodoru et al. (2007)
Thickness turbidite	30 cm	This study
Dry bulk density turbidite	0.4 g cm^{-3}	This study
Initial highly reactive Fe	350 µmol g^{-1}	This study
Rapidly sulfidized reactive Fe	200 µmol g^{-1}	This study
P loss from sediment	13 µmol g^{-1}	This study

reactive, non-sulfidized Fe of which ~200 µmol g^{-1} may be transformed during mass movement and early turbidite diagenesis. A previous estimate of the SW Black Sea area with turbidite intervals was 75 × 75 km (5625 km^2), based on the distance between two locations with similar turbidites (Yücel et al. 2010b). This constitutes ~ 30% of the SW deep basin. Using the more conservative estimate that our results may be representative for 10% of the SW deep basin, the upper turbidite interval at station 1 represents a total transport of ~1.3 Tg of highly reactive Fe into the SW deep basin of which ~ 0.7 Tg can be rapidly sulfidized (i.e. within a few decades). The total annual highly reactive burial Fe flux in the Black Sea deep basin is estimated to be ~ 6 Tg Fe yr^{-1} from deep-sea sediment traps (Muramoto et al. 1991) and Fe mass balance calculations (Anderson and Raiswell 2004). This comparison suggests that turbidity currents represent an episodic, yet recurring and quantitatively significant Fe burial in the Black Sea deep basin.

Assuming that all highly reactive Fe eventually forms FeS$_2$ in the water column or sediment and is subsequently buried (i.e. a molar Fe:S ratio of burial fluxes of 1:2), the input of highly reactive and rapidly sulfidized Fe during deposition of the 8-cm thick uppermost turbidite translates to additional pyrite-S burial of ~1.4 and 0.8 Tg, respectively. This is similar to recent estimates for the total annual S burial flux of 1 Tg y^{-1} in the anoxic zone of the Black Sea (Neretin et al. 2001) and a total reduced inorganic S flux into the deep basin of 2.5 Tg y^{-1} (Muramoto et al. 1991). In our calculations, we include only a small portion of the Black Sea deep basin area (10% of deep SW Black Sea, ~1% of the total area deep Black Sea floor). Based on our calculations for the 20-year period represented by the uppermost turbidite interval and the overlying surface sediment, turbidity currents contributed ~ 1% to total highly reactive Fe burial flux and ~ 5% to the total S burial flux during this period. We observed similar thicknesses for the normal marine and turbidite intervals at ~ 10–20 cm sediment depth below the uppermost turbidite interval. This suggests that the calculated contribution of turbidity currents to deep basin Fe and S fluxes may be representative for deep SW Black Sea sedimentation, at least for the period captured in the surface sediment core from station 1. As mentioned, the widespread occurrence of geochemically similar turbidite intervals in the deep SW Black Sea basin may point to the ubiquitous nature of such deposits. In addition, the uppermost turbidite interval at station 1 was relatively thin (~8 cm) compared to previous findings of 17–20 cm thick turbidite intervals immediately beneath the surface sediment in the SW Black Sea (Crusius and Anderson 1992; Yücel et al. 2010b). Yücel et al. (2010b) estimated that sulfidation of Fe in turbidity currents represented ~15% of total annual sulfur burial. Therefore, these fluxes could become much more significant when accurate assessments are made of the areal coverage and volumes of turbidite intervals in the deep Black Sea basin.

4.3.3. Impact of turbidite deposition on sedimentary Fe signatures

Non-turbidite deep Black Sea sediments generally are characterized by elevated Fe$_T$/Al and Fe$_{HR}$/Fe$_T$ ratios as a result of shelf-to-basin Fe shuttling: Fe mobilized from shelf sediments is transported into the deep basin where it is sequestered and buried as iron sulfide (e.g. Wijsman et al. 2001; Lyons and Severmann 2006). This shelf-to-basin shuttling constitutes a source of highly reactive Fe in addition to the Fe flux associated with the deposition of terrigenous material. Moving away from the shelf, the relative contribution of terrigenous Fe diminishes and Fe$_T$/Al and Fe$_{HR}$/Fe$_T$ ratios increase (Lyons and Severmann 2006). Comparing the Fe chemistry at slope station 13 to that at deep Black Sea station 2 where no turbidites were observed in the multi-core sediment record (Table 1), we find markedly higher Fe$_T$/Al and Fe$_{HR}$/Fe$_T$ ratios for normal marine sediment in the deep basin compared to the slope sediment (Table 6). The Fe$_T$/Al and Fe$_{HR}$/Fe$_T$ ratios for the turbidite material at station 1 are not significantly different from those in the source material, as previously observed by Lyons and Berner (1992) for turbidite layers at a similar depth (station

Table 6
Ratios of total Fe to Al (Fe_T/Al, in wt% wt%$^{-1}$) and highly reactive Fe to total Fe (Fe_{HR}/Fe_T, in mol mol^{-1}) and degree of pyritization (DOP) (sulfidation for station 13) for sediments from stations 1, 2 and 13. The average is given, with the standard deviation between parentheses. For station 1, the averages are calculated for the top two turbidite intervals.

	Fe_T/Fe_{Al}			Fe_{HR}/Fe_T			DOP		
	13 (slope)	1 (turb)	2 (deep)	13 (slope)	1 (turb)	2 (deep)	13 (slope)	1 (turb)	2 (deep)
average	0.56	0.54	0.96	0.48	0.47	0.73	0.07	0.61	0.86
(st. dev.)	(0.01)	(0.03)	(0.09)	(0.02)	(0.03)	(0.08)	(0.01)	(0.03)	(0.04)

7 of the 1988 Knorr expedition, ~1950 mbss) in the south-west Black Sea. This shows that (highly reactive) Fe enrichment does not occur during transport and deposition of turbidites. As such, the Fe chemical signatures of shelf-to-basin Fe shuttling are not recorded during turbidite deposition. Interestingly, Lyons and Berner (1992) found a similar degree of Fe sulfidation in the source sediment (described to be black, sulfidic muds from the euxinic upper shelf, ~200 mbss) and the turbidite intervals in their southern Black Sea stations. By contrast, we found much higher DOP in the station 1 turbidite intervals (~0.6) compared to the slope station 13 source material (< 0.1). These results together show that the impact of turbidite deposition on Black Sea biogeochemical cycling and particularly S burial strongly depends on the geochemical character of the source sediment, which can vary spatially and temporally. Regardless, the similar Fe chemistry with abundant Fe (III) in the source sediment found here and by Yücel et al. (2010b) for a different deep SW Black Sea station suggest that rapid injection of large amounts of unsulfidized Fe(III) and Fe(II) may be a widespread process in the deep Black Sea.

4.4. The impact of turbidity currents on Black Sea P cycling

Our geochemical characterizations also allow us to explore the impact of turbidity currents on the Black Sea P cycle. On average, total P contents in station 1 sediments are 45% (or 13 μmol g^{-1}) lower than in sediments from station 13 (Fig. 7). This decrease can almost exclusively be attributed to a strong decline in CDB-P at station 1. The nature of the CDB-P pool can be complex with contributions from a variety of P phases such as P bound to easily reducible Fe(III) (oxyhydr) oxides, Fe(II) phosphates, and clay- and $CaCO_3$-bound P (Kraal et al. 2017; Dijkstra et al. 2018b). Conversely, CDB-Fe represents easily reducible Fe(III) (oxyhydr)oxides (Ruttenberg 1992) and possibly labile Fe(II) phases. The near-complete depletion of CDB-Fe indicates efficient reductive dissolution and sulfidation of these phases and subsequent release of P. The remaining CDB-P in the turbidite intervals at station 1 likely consists of $CaCO_3$-associated P and, considering the abundance of HCl-Fe(II), possibly P associated with remaining Fe(II) phases.

To calculate P fluxes, we use the same parameters as used for Fe transport (Table 5). Furthermore, comparing P contents in sediments from station 13 and station 1 indicates that equal parts of P are released from and buried with turbidites in the SW Black Sea deep basin. Consequently, we calculate equal total P release and P burial associated with the most recent turbidite interval of ~ 0.015 Tg P. For comparison, a recent estimate for the modern P burial flux in the deep (> 1800 mbss) Black Sea basin based on non-turbidite sediments is 0.005 Tg y^{-1} (Teodoru et al. 2007). Additionally, using a recent estimate for diffusive P release from non-turbidite deep basin sediments (2920 μmol m^{-2} y^{-1}) (Dijkstra et al. 2018b) we calculate total diffusive benthic P release in the deep Black Sea to be ~0.02 Tg y^{-1}. This would imply that over the last 20 years, a period that seems representative for recent sedimentation in the deep Black Sea (see Section 4.3), P burial from deposition of turbidites (0.015 Tg) was ~15% of P burial from normal marine sedimentation (0.1 Tg P). Assuming that the benthic efflux is representative for deep Black Sea sediments, the calculations further suggest that during this time period, P release from turbidity

currents was ~ 5% of the total diffusive release from non-turbidite sediments over the last 20 years: 0.015 Tg P versus 0.5 Tg P, respectively. As such, variations in the turbidite deposition have the potential to affect the deep Black Sea P budget.

5. Implications

We find that turbidity currents can significantly alter the budgets of Fe, P and S in the deep Black Sea. Even though we have restricted our calculations to a small area in the south-west Black Sea, we found that episodic burial fluxes of Fe and S associated with the introduction and sulfidation of highly reactive Fe phases from turbidites in the sulfidic deep waters can contribute significantly to Fe and S burial fluxes. Furthermore, we calculate that the release of P during and after turbidite deposition due to reductive dissolution of P-bearing Fe phases in the sulfidic deep basin may be an order of magnitude greater than the total efflux of P from the sediment in the deep Black Sea. Our findings stress the need for more detailed insight into the distribution of turbidite intervals in the Black Sea in order to better assess their potentially prominent role in the fluxes and budgets of essential elements such as Fe, P and S.

Furthermore, we show that the reactivity of non-sulfidized Fe phases towards the high concentrations of dissolved HS- in the waters and sediments of the deep Black Sea may be lower than expected. This does not only affect the extent to and timescales over which turbidity currents may affect sediment geochemistry, but also suggests that sediment redox chemistry that is out of equilibrium with extant depositional conditions may be in fact be preserved longer than expected. This can directly impact the interpretation of paleorecords as archives of depositional conditions.

References

Aller, R.C., 1998. Mobile deltaic and continental shelf muds as suboxic, fluidized bed reactors. Mar. Chem. 61 (3–4), 143–155.
Anderson, T.F., Raiswell, R., 2004. Sources and mechanisms for the enrichment of highly

reactive iron in euxinic Black Sea sediments. Am. J. Sci. 304 (3), 203–233.

APHA, 2005. Standard Methods for the Examination of Water and Wastewater. American Public Health Association - American Water Works Association - Water Environment Federation.

Berner, R.A., 1970. Sedimentary pyrite formation. Am. J. Sci. 268 (1), 1–23.

Boesen, C., Postma, D., 1988. Pyrite formation in anoxic environments of the Baltic. Am. J. Sci. 288 (6), 575–603.

Boudreau, B.P., 1997. Diagenetic Models and their Implementation: Modelling Transport and Reactions in Aquatic Sediments. Springer-Verlag.

Boyd, P.W., Ellwood, M.J., 2010. The biogeochemical cycle of iron in the ocean. Nat. Geosci. 3, 675.

Boyd, P.W., Ellwood, M.J., Tagliabue, A., Twining, B.S., 2017. Biotic and abiotic retention, recycling and remineralization of metals in the ocean. Nat. Geosci. 10 (3), 167–173.

Brendel, P.J., Luther III, G.W., 1995. Development of a gold amalgam voltammetric microelectrode for the determination of dissolved Fe, Mn, O2, and S(-II) in porewaters of marine and freshwater sediments. Environ. Sci. Technol. 29 (3), 751–761.

Burdige, D.J., Komada, T., 2013. Using ammonium pore water profiles to assess stoichiometry of deep remineralization processes in methanogenic continental margin sediments. Geochem. Geophys. Geosyst. 14 (5), 1626–1643.

Canfield, D.E., Raiswell, R., Bottrell, S.H., 1992. The reactivity of sedimentary iron minerals toward sulfide. Am. J. Sci. 292 (9), 659–683.

Canfield, D.E., Lyons, T.W., Raiswell, R., 1996. A model for iron deposition to euxinic Black Sea sediments. Am. J. Sci. 296 (7), 818–834.

Claff, S.R., Sullivan, L.A., Burton, E.D., Bush, R.T., 2010. A sequential extraction procedure for acid sulfate soils: Partitioning of iron. Geoderma 155 (3–4), 224–230.

Codispoti, L.A., Friederich, G.E., Murray, J.W., Sakamoto, C.M., 1991. Chemical variability in the Black Sea: implications of continuous vertical profiles that penetrated the oxic/anoxic interface. Deep Sea Res. 38 (Supplement 2 (0)), S691–S710.

Crusius, J., Anderson, R.F., 1992. Inconsistencies in accumulation rates of Black Sea sediments inferred from records of laminae and ²¹⁰Pb. Paleoceanography 7 (2), 215–227.

Dale, A.W., Brüchert, V., Alperin, M., Regnier, P., 2009. An integrated sulfur isotope model for Namibian shelf sediments. Geochim. Cosmochim. Acta 73 (7), 1924–1944.

Degens, E.T., Ross, D.A., 1974. The Black Sea—Geology, Chemistry, and Biology. Vol. 20. American Association of Petroleum Geologists Memoir, pp. 633.

Dijkstra, N., Kraal, P., Kuypers, M.M.M., Schnetger, B., Slomp, C.P., 2014. Are iron-phosphate minerals a sink for phosphorus in anoxic Black Sea sediments? PLoS One 9 (7), e101139.

Dijkstra, N., Hagens, M., Egger, M., Slomp, C.P., 2018a. Post-depositional formation of vivianite-type minerals alters sediment phosphorus records. Biogeosciences 15 (3), 861–883.

Dijkstra, N., Kraal, P., Séguret, M.J.M., Flores, M.R., Gonzalez, S., Rijkenberg, M.J.A., Slomp, C.P., 2018b. Phosphorus dynamics in and below the redoxcline in the Black Sea and implications for phosphorus burial. Geochim. Cosmochim. Acta 222, 685–703 Supplement C.

Eckert, S., Brumsack, H.-J., Severmann, S., Schnetger, B., März, C., Fröllje, H., 2013. Establishment of euxinic conditions in the Holocene Black Sea. Geology 41 (4), 431–434.

Egger, M., Kraal, P., Jilbert, T., Sulu-Gambari, F., Sapart, C.J., Röckmann, T., Slomp, C.P., 2016. Anaerobic oxidation of methane alters sediment records of sulfur, iron and phosphorus in the Black Sea. Biogeosciences 13 (18), 5333–5355.

Grashoff, K., Erhardt, M., Kremling, K.e., 1983. Methods of Seawater Analysis, Second Edition. Verlag Chemie, Weinheim/Deerfield Beach, Florida.

Grégoire, M., Beckers, J.M., Nihoul, J.C.J., Stanev, E., 1998. Reconnaissance of the main Black Sea's ecohydrodynamics by means of a 3D interdisciplinary model. J. Mar. Syst. 16 (1–2), 85–105.

Hardisty, D.S., Lyons, T.W., Riedinger, N., Isson, T.T., Owens, J.D., Aller, R.C., Rye, D.M., Planavsky, N.J., Reinhard, C.T., Gill, B.C., Masterson, A.L., Asael, D., Johnston, D.T., 2018. An evaluation of sedimentary molybdenum and iron as proxies for pore fluid paleoredox conditions. Am. J. Sci. 318 (5), 527–556.

Helder, W., De Vries, R.T.P., 1979. An automatic phenol-hypochlorite method for the determination of ammonia in sea- and brackish waters. Neth. J. Sea Res. 13 (1), 154–160.

Jilbert, T., Slomp, C.P., 2013. Iron and manganese shuttles control the formation of authigenic phosphorus minerals in the euxinic basins of the Baltic Sea. Geochim. Cosmochim. Acta 107 (0), 155–169.

Konovalov, S.K., Luther Iii, G.W., Yücel, M., 2007. Porewater redox species and processes in the Black Sea sediments. Chem. Geol. 245 (3–4), 254–274.

Konuk, Y.T., Ergün, M., Avci, M., Duman, M., 1991. The effects of neotectonic movements on the recent sedimentation of the SW Black Sea. In: İzdar, E., Murray, J.W. (Eds.), Black Sea Oceanography. Springer Netherlands, Dordrecht, pp. 389–400.

Kraal, P., Slomp, C.P., 2014. Rapid and extensive alteration of phosphorus speciation during oxic storage of wet sediment samples. PLoS One 9 (5), e96859.

Kraal, P., Slomp, C.P., Forster, A., Kuypers, M.M.M., Sluijs, A., 2009. Pyrite oxidation during sample storage determines phosphorus fractionation in carbonate-poor anoxic sediments. Geochim. Cosmochim. Acta 73 (11), 3277–3290.

Kraal, P., Burton, E.D., Bush, R.T., 2013. Iron monosulfide accumulation and pyrite formation in eutrophic estuarine sediments. Geochim. Cosmochim. Acta 122 (0), 75–88.

Kraal, P., Dijkstra, N., Behrends, T., Slomp, C.P., 2017. Phosphorus burial in sediments of the sulfidic deep Black Sea: key roles for adsorption by calcium carbonate and apatite authigenesis. Geochim. Cosmochim. Acta 204, 140–158.

Lenstra, W.K., Hermans, M., Séguret, M.J.M., Witbaard, R., Behrends, T., Dijkstra, N., van Helmond, N.A.G.M., Kraal, P., Laan, P., Rijkenberg, M.J.A., Severmann, S., Teacă, A., Slomp, C.P., 2018. The shelf-to-basin iron shuttle in the Black Sea revisited. Chem. Geol. https://doi.org/10.1016/j.chemgeo.2018.10.024. In press.

Lenz, C., Jilbert, T., Conley, D.J., Slomp, C.P., 2015. Hypoxia-driven variations in iron and manganese shuttling in the Baltic Sea over the past 8 kyr. Geochem. Geophys. Geosyst. 16 (10), 3754–3766.

Lericolais, G., Bourget, J., Popescu, I., Jermannaud, P., Mulder, T., Jorry, S., Panin, N., 2013. Late quaternary deep-sea sedimentation in the western Black Sea: new insights from recent coring and seismic data in the deep basin. Glob. Planet. Chang. 103, 232–247.

Lord, C.J., 1982. A selective and precise method for pyrite determination in sedimentary materials. J. Sediment. Res. 52 (2), 664–666.

Luther III, G.W., Brendel, P.J., Lewis, B.L., Sundby, B., Lefrançois, L., Silverberg, N., Nuzzio, D.B., 1998. Simultaneous measurement of O2, Mn, Fe, I-, and S(-II) in marine pore waters with a solid-state voltammetric microelectrode. Limnol. Oceanogr. 43 (2), 325–333.

Luther III, G.W., Glazer, B.T., Ma, S., Trouwborst, R.E., Moore, T.S., Metzger, E., Kraiya, C., Waite, T.J., Druschel, G., Sundby, B., Taillefert, M., Nuzzio, D.B., Shank, T.M., Lewis, B.L., Brendel, P.J., 2008. Use of voltammetric solid-state (micro)electrodes for studying biogeochemical processes: Laboratory measurements to real time measurements with an in situ electrochemical analyzer (ISEA). Mar. Chem. 108 (3-4), 221–235.

Luther III, G.W., Rickard, D.T., 2005. Metal sulfide cluster complexes and their biogeochemical importance in the environment. J. Nanopart. Res. 7 (4–5), 389–407.

Luther III, G.W., Glazer, B.T., Hohmann, L., Popp, J.I., Taillefert, M., Rozan, T.F., Brendel, P.J., Theberge, S.M., Nuzzio, D.B., 2001. Sulfur speciation monitored with solid state gold amalgam voltammetric microelectrodes: polysulfides as a special case in sediments, microbial mats and hydrothermal vent waters. J. Environ. Monit. 3 (1), 61–66.

Lyons, T.W., 1997. Sulfur isotopic trends and pathways of iron sulfide formation in upper Holocene sediments of the anoxic Black Sea. Geochim. Cosmochim. Acta 61 (16), 3367–3382.

Lyons, T.W., Berner, R.A., 1992. Carbon-sulfur-iron systematics of the uppermost deep-water sediments of the Black Sea. Chem. Geol. 99, 1–3), 1-27.

Lyons, T.W., Severmann, S., 2006. A critical look at iron paleoredox proxies: New insights from modern euxinic marine basins. Geochim. Cosmochim. Acta 70 (23), 5698–5722.

McAnena, A., 2011. The Reactivity and Isotopic Fractionation of Fe-Bearing Minerals during Sulfidation: An Experimental Approach. PhD Thesis. Newcastle University, Newcastle.

Muramoto, J.A., Honjo, S., Fry, B., Hay, B.J., Howarth, R.W., Cisne, J.L., 1991. Sulfur, iron and organic carbon fluxes in the Black Sea: sulfur isotopic evidence for origin of sulfur fluxes. Deep Sea Res. 38, S1151–S1187.

Murphy, J., Riley, J.P., 1962. A modified single solution method for the determination of phosphate in natural waters. Anal. Chim. Acta 27, 31–36.

Nembrini, G.P., Capobianco, J.A., Viel, M., Williams, A.F., 1983. A Mössbauer and chemical study of the formation of vivianite in sediments of Lago Maggiore (Italy). Geochim. Cosmochim. Acta 47 (8), 1459–1464.

Neretin, L.N., Volkov, I.I., Böttcher, M.E., Grinenko, V.A., 2001. A sulfur budget for the Black Sea anoxic zone. Deep Sea Res. Pt. 1 48 (12), 2569–2593.

Oaie, G., Secrieru, D., Shimkus, K., 2005. Black Sea Basin: sediment types and distribution, sedimentation processes. Geoecomarina 9 (10), 21–30.

Poulton, S.W., Canfield, D.E., 2005. Development of a sequential extraction procedure for iron: implications for iron partitioning in continentally derived particulates. Chem. Geol. 214 (3–4), 209–221.

Poulton, S.W., Canfield, D.E., 2011. Ferruginous conditions: a dominant feature of the ocean through Earth's history. Elements 7 (2), 107–112.

Poulton, S.W., Krom, M.D., Raiswell, R., 2004. A revised scheme for the reactivity of iron (oxyhydr)oxide minerals towards dissolved sulfide. Geochim. Cosmochim. Acta 68 (18), 3703–3715.

Raiswell, R., Berner, R.A., 1985. Pyrite formation in euxinic and semi-euxinic sediments. Am. J. Sci. 285 (8), 710–724.

Raiswell, R., Canfield, D.E., 1998. Sources of iron for pyrite formation in marine sediments. Am. J. Sci. 298 (3), 219–245.

Raiswell, R., Buckley, F., Berner, R.A., Anderson, T.F., 1988. Degree of pyritization of iron as a paleoenvironmental indicator of bottom-water oxygenation. J. Sediment. Res. 58 (5), 812–819.

Reichart, G.J., Den Dulk, M., Visser, H.J., Van der Weijden, C.H., Zachariasse, W.J., 1997. A 225 kyr record of dust supply, paleoproductivity and the oxygen minimum zone from the Murray ridge (northern Arabian Sea). Palaeogeogr. Palaeocl. 134 (1–4), 149–169.

Rickard, D., Luther, G.W., 2007. Chemistry of iron sulfides. Chem. Rev. 107, 514–562.

Ruttenberg, K.C., 1992. Development of a sequential extraction method for different forms of phosphorus in marine sediments. Limnol. Oceanogr. 37 (7), 1460–1482.

Scholz, F., 2018. Identifying oxygen minimum zone-type biogeochemical cycling in Earth history using inorganic geochemical proxies. Earth-Sci. Rev. 184, 29–45.

Scholz, F., McManus, J., Mix, A.C., Hensen, C., Schneider, R.R., 2014a. The impact of ocean deoxygenation on iron release from continental margin sediments. Nat. Geosci. 7 (6), 433–437.

Scholz, F., Severmann, S., McManus, J., Hensen, C., 2014b. Beyond the Black Sea paradigm: the sedimentary fingerprint of an open-marine iron shuttle. Geochim. Cosmochim. Acta 127, 368–380.

Severmann, S., Lyons, T.W., Anbar, A., McManus, J., Gordon, G., 2008. Modern iron isotope perspective on the benthic iron shuttle and the redox evolution of ancient oceans. Geology 36 (6), 487–490.

Slomp, C.P., Epping, E.H.G., Helder, W., Van Raaphorst, W., 1996. A key role for iron-bound phosphorus in authigenic apatite formation in North Atlantic continental platform sediments. J. Mar. Res. 54 (6), 1179–1205.

Sorokin, Y.I., 1983. The Black Sea. In: Ketchum, B.H. (Ed.), Estuaries and Enclosed Seas. Elsevier, New York, pp. 253–292.

Strokal, M., Kroeze, C., 2013. Nitrogen and phosphorus inputs to the Black Sea in

1970–2050. Reg. Environ. Chang. 13 (1), 179–192.

Tagliabue, A., Bowie, A.R., Boyd, P.W., Buck, K.N., Johnson, K.S., Saito, M.A., 2017. The integral role of iron in ocean biogeochemistry. Nature 543 (7643), 51–59.

Taillefert, M., Neuhuber, S., Bristow, G., 2007. The effect of tidal forcing on biogeochemical processes in intertidal salt marsh sediments. Geochem. T. 8. https://doi.org/10.1186/1467-4866-8-6.

Teodoru, C.R., Friedl, G., Friedrich, J., Roehl, U., Sturm, M., Wehrli, B., 2007. Spatial distribution and recent changes in carbon, nitrogen and phosphorus accumulation in sediments of the Black Sea. Mar. Chem. 105 (1–2), 52–69.

Tolmazin, D., 1985a. Changing coastal oceanography of the Black Sea II: Mediterranean effluent. Prog. Oceanogr. 15 (4), 277–316.

Tolmazin, D., 1985b. Changing Coastal oceanography of the Black Sea. I: Northwestern Shelf. Prog. Oceanogr. 15 (4), 217–276.

Tugrul, S., Besiktepe, T., Salihoglu, I., 2002. Nutrient exchange fluxes between the Aegean and Black Seas through the Marmara Sea. Mediterr. Mar. Sci. 3 (1), 10.

Turekian, K.K., Wedepohl, K.H., 1961. Distribution of the elements in some major units of the Earth's crust. Geol. Soc. Am. Bull. 72 (2), 175–192.

Wijsman, J.W.M., Middelburg, J.J., Heip, C.H.R., 2001. Reactive iron in Black Sea Sediments: implications for iron cycling. Mar. Geol. 172 (3–4), 167–180.

Wilkin, R.T., Arthur, M.A., Dean, W.E., 1997. History of water-column anoxia in the Black Sea indicated by pyrite framboid size distributions. Earth Planet. Sci. Lett. 148 (3), 517–525.

Yücel, M., 2013. Down the thermodynamic ladder: A comparative study of marine redox gradients across diverse sedimentary environments. Estuar. Coast. Shelf S. 131, 83–92.

Yücel, M., Konovalov, S.K., Moore, T.S., Janzen, C.P., Luther Iii, G.W., 2010a. Sulfur speciation in the upper Black Sea sediments. Chem. Geol. 269 (3–4), 364–375.

Yücel, M., Luther Iii, G.W., Moore, W.S., 2010b. Earthquake-induced turbidite deposition as a previously unrecognized sink for hydrogen sulfide in the Black Sea sediments. Mar. Chem. 121 (1–4), 176–186.

Yücel, M., Moore, W.S., Butler, I.B., Boyce, A., Luther Iii, G.W., 2012. Recent sedimentation in the Black Sea: New insights from radionuclide distributions and sulfur isotopes. Deep Sea Res. Pt. 1 66, 103–113.